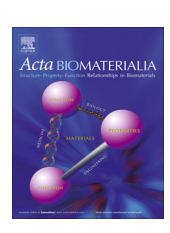
ELSEVIER

Contents lists available at ScienceDirect

Acta Biomaterialia

journal homepage: www.elsevier.com/locate/actabiomat



Full length article

Controlled-temperature photothermal and oxidative bacteria killing and acceleration of wound healing by polydopamine-assisted Au-hydroxyapatite nanorods



Xiaomo Xu^a, Xiangmei Liu^a, Lei Tan^a, Zhenduo Cui^b, Xianjin Yang^b, Shengli Zhu^b, Zhaoyang Li^b, Xubo Yuan^b, Yufeng Zheng^c, Kelvin Wai Kwok Yeung^d, Paul K. Chu^e, Shuilin Wu^{a,b,*}

- ^a Hubei Collaborative Innovation Center for Advanced Organic Chemical Materials, Ministry-of-Education Key Laboratory for the Green Preparation and Application of Functional Materials, Hubei Key Laboratory of Polymer Materials, School of Materials Science & Engineering, Hubei University, Wuhan 430062, China
- b School of Materials Science & Engineering, The Key Laboratory of Advanced Ceramics and Machining Technology by the Ministry of Education of China, Tianjin University, Tianjin 300072, China
- c State Key Laboratory for Turbulence and Complex System and Department of Materials Science and Engineering, College of Engineering, Peking University, Beijing 100871, China
- d Department of Orthopaedics & Traumatology, Li Ka Shing Faculty of Medicine, The University of Hong Kong, Pokfulam, Hong Kong, China
- e Department of Physics & Department of Materials Science and Engineering, City University of Hong Kong, Tat Chee Avenue, Kowloon, Hong Kong, China

ARTICLE INFO

Article history:
Received 22 April 2018
Received in revised form 14 July 2018
Accepted 16 July 2018
Available online 17 July 2018

Keywords:
Au
Hydroxyapatite
Controlled temperature photothermal
therapy
Wound healing
Antibacterial

ABSTRACT

Since skin wounds are subject to bacterial infection and tissue regeneration may be impeded, there is demand for biomaterials that possess rapid bactericidal and tissue repair capability. Herein we report in situ promotion of wound healing by a photothermal therapy (PTT) assisted nanocatalytic antibacterial system utilizing a polydopamine (PDA) coating on hydroxyapatite (HAp) incorporated with gold nanoparticles (Au-HAp). The PDA@Au-HAp NPs produce hydroxyl radicals (\cdot OH) via catalysis of a small concentration of H_2O_2 to render bacteria more vulnerable to the temperature change. The antibacterial efficacy against Escherichia coli and Staphylococcus aureus is 96.8% and 95.2%, respectively, at a controlled photo-induced temperature of 45 °C that causes no damage to normal tissues. By combining catalysis with near-infrared (NIR) photothermal therapy, the PDA@Au-HAp NPs provide safe, rapid, and effective antibacterial activity compared to \cdot OH or PTT alone. In addition, this system stimulates the tissue repairing-related gene expression to facilitate the formation of granulation tissues and collagen synthesis and thus accelerate wound healing. After the 10-day treatment of skin wounds $in\ vivo$, PDA@Au-HAp group exhibits quicker recovery than the control group and both sterilization and healing are completed after the 10-day treatment.

Statement of significance

This study presents *in situ* promotion of wound healing by a low-temperature photothermal therapy (PTT) assisted nanocatalytic antibacterial system utilizing a polydopamine (PDA) coating on hydroxyapatite (HAp) incorporated with gold nanoparticles (Au-HAp). The PDA@Au-HAp NPs produce hydroxyl radicals (.OH) via catalysis of a small concentration of H_2O_2 to render bacteria more vulnerable to temperature change. After irradiation by 808 nm laser, the antibacterial efficacy against *Escherichia coli* ($E.\ coli$) and *Staphylococcus aureus* ($S.\ aureus$) is 96.8% and 95.2%, respectively, at a low photo-induced temperature of 45 °C which causes no damage to normal tissues. In addition, this system stimulates the tissue repairing-related gene expression to facilitate the formation of granulation tissues and collagen synthesis and accelerate wound healing.

© 2018 Acta Materialia Inc. Published by Elsevier Ltd. All rights reserved.

1. Introduction

Microbial infection which can cause serious complications after surgery and during wound healing usually occurs at damaged tissues [1–4], and it is important to accelerate tissue regeneration in order to minimize the possibility of bacterial infection [5]. The

E-mail address: shuilinwu@tju.edu.cn (S. Wu).

^{*} Corresponding author at: School of Materials Science & Engineering, The Key Laboratory of Advanced Ceramics and Machining Technology by the Ministry of Education of China, Tianjin University, Tianjin 300072, China.

most widely used method to combat bacterial infection is antibiotics therapy [6–8], but overuse and abuse of antibiotics can generate bacterial resistance inevitably reducing the treatment effectiveness and even spurring the development superbacteria [9,10]. Therefore, it is urgent to develop a new wound therapy with antibacterial effects.

Photothermal therapy (PTT) is based on the ability to convert light into heat to destroy microorganisms such as bacteria thermally [11–13]. PTT triggered by near-infrared (NIR) light usually requires a temperature of 50 °C or higher to denature proteins and kill microbes because cell damage such as apoptosis at a lower temperature (e.g., 45 °C) can be repaired, but the high temperature may cause inflammation and thermal damage to nearby tissues [14,15]. Therefore, a bactericidal strategy at a lower temperature is more desirable. Polydopamine (PDA) is well known for selfpolymerization of dopamine to form surface-adherent nanocoatings on a wide range of materials [16]. In addition, PDA which has latent photothermal effects and excellent biocompatibility is a photothermal therapeutic agent that can reach 58 °C during cancer treatment in vivo and the chemical functional groups can be exploited [17,18]. Nevertheless, the high bactericidal temperature damages normal tissues and in fact, a simple antibacterial mechanism based on nanomaterials is not effective in eradicating bacteria totally [19,20].

As one of the most lethal reactive oxygen species (ROS), the hydroxyl radical (.OH) has high antibacterial activity and no bacterial resistance, because there is no detoxifying cell enzyme [21]. .OH can induce initial oxidative damage to cell wall and membrane and in combination with PTT, the damaged membrane has improved permeability and sensitivity to heat and the treatment time and side effects of PTT can be reduced [22,23]. The supporting role of H₂O₂ in dermal wound healing is subject to redox control and H₂O₂ is a relatively poorly reactive ROS, which allows it to migrate further from its site of generation to serve as a signaling molecule or second messenger [24,25]. Although H₂O₂ is a common antibacterial agent, the disinfectant concentration of H₂O₂ of 0.5-3% may hinder wound healing and even damage normal tissues [26]. The use of V_2O_5 , iron oxide, and graphene quantum dots (GQD) to catalyze the formation of ROS from H₂O₂ to enhance the antibacterial performance has been reported [27-29]. Au nanoparticles (NPs), widely used nanomaterials with attractive optical and electronic properties as well as excellent biocompatibility [30,31], have unique catalytic properties [32,33]. Hence, it is possible that AuNPs-based hybrid materials can catalyze the decomposition of small concentrations of H_2O_2 to generate hydroxyl radicals (.OH). Hydroxyapatite (HAp) is a widely accepted bioactive material, which can not only affect the cell behaviors but also form a phosphate layer to adsorb protein molecules to benefit cell adhesion, proliferation, and differentiation [34,35].

In this work, a bifunctional hybrid system composed of Au NPs in conjunction with PDA-assisted HAp (PDA@Au-HAp) is designed and prepared to accelerate tissue regeneration and disinfect wounds at the same time. The PDA@Au-HAp NPs not only promote the expression of related genes in NIH3T3 cells, but also facilitate the formation of granulation tissue and collagen synthesis to accelerate wound healing. Production of .OH *via* catalytic decomposition of H₂O₂ at a low concentration enhances the photothermal effects to achieve high antibacterial efficacy at a controlled temperature of 45 °C in a short treatment time so as to avoid damage to normal tissues. The mechanism is schematically illustrated in Fig. 1.

2. Materials and methods

2.1. Synthesis of hydroxyapatite nanorods

The hydroxyapatite nanorods (HAp) were synthesized by a hydrothermal method. Typically, the 0.5 M aqueous solution of

 $Ca(NO_3)_2 \cdot 4H_2O$ and 0.3 M aqueous solution of $(NH_4)_2HPO_4$ were mixed with a molar ratio of Ca:P=1:1.67 and adjusted to a pH of 8.7 with 25% ammonia. The mixture was put in a Teflon-lined stainless steel autoclave and heated to 130 °C for 12 h. After the reaction, the precipitate was separated by centrifugation, then washed with deionized (DI) water three times until neutral, freeze-dried, and calcined at 400 °C for 5 h.

2.2. Synthesis of Au-HAp

The Au nanoparticles (NPs) were deposited on HAp by a deposition–precipitation method. $0.06\,\mathrm{g}$ of $\mathrm{HAuCl_4.3H_2O}$ were dissolved in 45 mL of DI water at a pH of 9 by adding $0.1\,\mathrm{M}$ NaOH under vigorous stirring. $0.75\,\mathrm{g}$ of HAp were added to the HAuCl₄ aqueous solution and the pH was adjusted to 9 with NaOH. After vigorous stirring for 1 h, the product was heated to $65\,^{\circ}\mathrm{C}$ and stirred for another 1 h. The precipitate was filtered and washed with DI water until it was free of chloride ions, dried at $60\,^{\circ}\mathrm{C}$ overnight, and calcined at $500\,^{\circ}\mathrm{C}$ for 3 h for further use.

2.3. Synthesis of PDA@Au-HAp

0.5 g of the as-prepared Au-HAp were stirred in dopamine containing 1 mg/mL tris-buffer solution (100 mL, 10 mM; pH 8.5) for 24 h. The sample was separated by centrifugation, washed with DI water three times, and dried at 40 °C under vacuum.

2.4. Measurement and characterization

A transmission electron microscope (TEM; Tecnai G20, FEI, USA) was used to examine the size and morphology of the materials. The crystallinity and purity were determined by X-ray diffraction (XRD, D8A25, Bruker, Germany) using Cu K_{α} radiation (λ = 1.54051 and 1.54433 Å) over the 2θ range of $10-80^{\circ}$. The chemical composition was determined by Fourier-transform infrared spectroscopy (FTIR, Nicolet IS10, USA) and UV–Vis absorption spectra were recorded on the JASCO V550 UV/visible spectrophotometer (JASCO International Co., LTD., Tokyo, Japan). X-ray photoelectron spectroscopy (XPS, Thermo Fisher Scientific 250Xi) was performed to determine the chemical states.

2.5. Peroxidase-like activity measurement

The peroxidase-like activity of Au-HAp and PDA@Au-HAp was investigated by catalytic oxidation of the peroxidase substrate 3, 3' 5, 5'-tetramethylbenzidine (TMB) in the presence of $\rm H_2O_2$. Oxidation of TMB by Au-HAp/PDA@Au-HAp in 25 mM phosphate buffer (pH 4.0) produced a blue color with major absorbance peaks at 370 nm and 652 nm. The experiments were carried out with 200 $\mu g/mL$ Au-HAp and PDA@Au-HAp, and 0.8 mM TMB was added into the buffer solution (400 μL , pH 4.0, 37 °C) in the presence of $\rm H_2O_2$ (50 mM).

2.6. Detection of hydroxyl radicals (.OH)

The .OH radicals generated from H_2O_2 catalysis with Au-HAp and PDA@Au-HAp were evaluated by monitoring the fluorescence (FL) of 2-hydroxy terephthalic acid (TAOH) arising from oxidation of terephthalic acid (TA) in the aqueous solution. TA was reduced to TAOH by .OH with the maximum FL peak at 435 nm. Eight solutions (TA, H_2O_2 , Au-HAp, PDA@Au-HAp, TA + Au-HAp, TA + PDA@Au-HAp, TA + Au-HAp + H_2O_2) were investigated. 0.3 mL of the 200 µg/mL Au-HAp and PDA@Au-HAp aqueous solution, 0.3 mL of 1 mM H_2O_2 aqueous solution, and 0.3 mL of 5 mM TA aqueous solution were mixed with 0.3 mL of 1.0 M acetate buffer (pH = 4.0) or 0.01 M PBS buffer

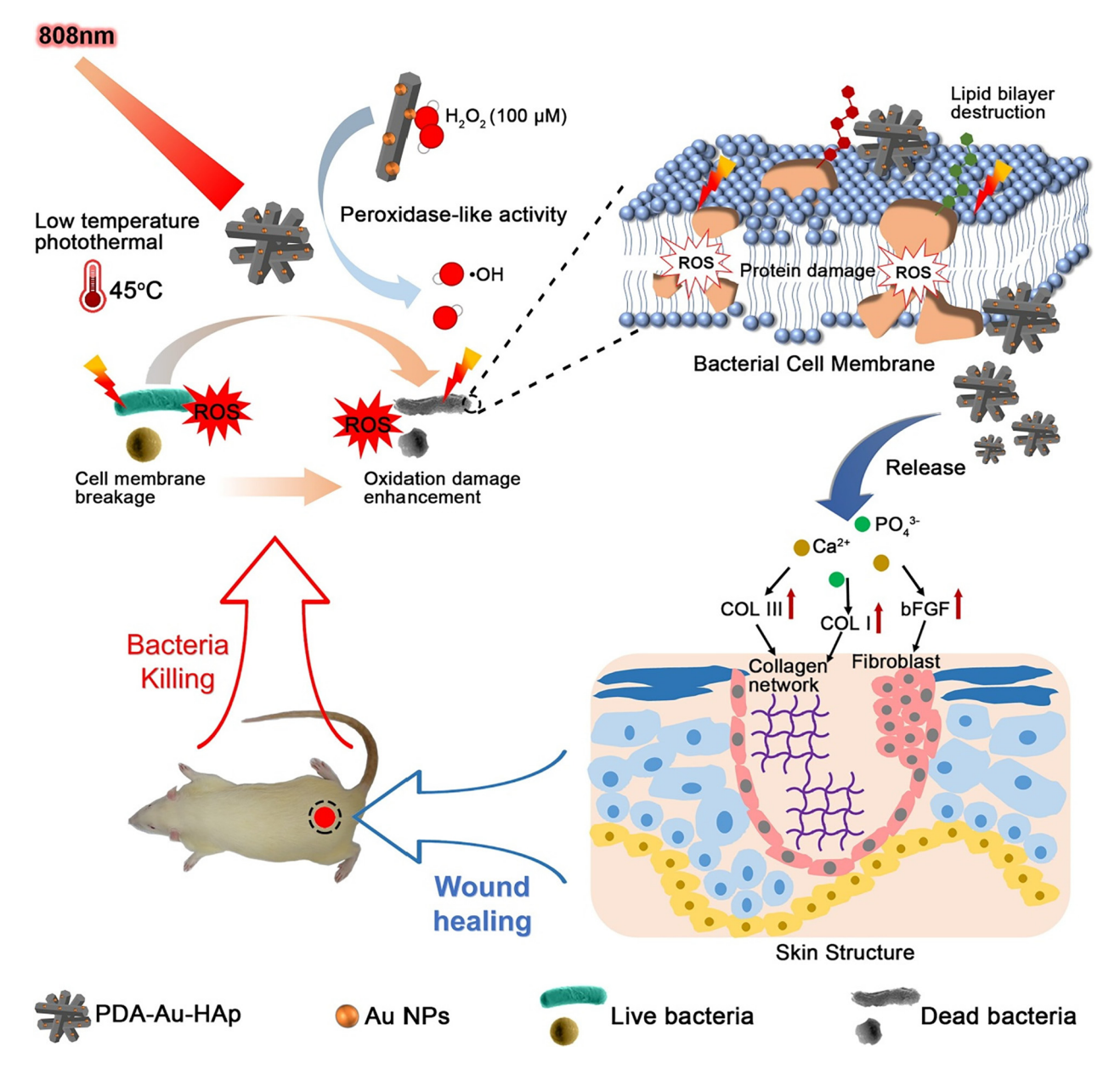


Fig. 1. Schematic illustration of photothermal therapy combined with catalysis to achieve antibacterial effects and promote wound healing *in vivo*. PDA@Au-HAp catalyze the formation of .OH from H_2O_2 at low concentration, enhanced photothermal antibacterial performance at 45 °C *via* destruct cell membranes, proteins and DNA, PDA and the release of Ca^{2+} and PO_4^{3-} promote the expression of related genes in NIH3T3 cells, facilitate the formation of granulation tissue and collagen synthesis to accelerate wound healing

(pH = 7.0) and diluted with DI water to 3 mL. The final concentrations were 20 $\mu g/mL$, 100 μM , 500 μM , and 100 μM for the Au-HAp or PDA@Au-HAp, H_2O_2 , TA, and acetate buffer, respectively. The mixture was gently shaken and stored at 37 °C for 12 h in the dark. Changes in the fluorescence emission at 435 nm were recorded.

2.7. Photothermal conversion efficiency (η) of PDA@Au-HAp

The photothermal conversion efficiency (η) of PDA@Au-HAp was calculated as follows. 500 μ L of the PDA@Au-HAp aqueous dispersion with different concentrations (0, 50, 100, 200, 500 and 1000 μ g mL⁻¹) were exposed to the 808 nm NIR laser for 10 min and the laser was turned off to let the solution cool to room temperature. The heating and cooling temperature patterns of one sample (200 μ g mL⁻¹) were recorded on a thermal camera (FLIR, E50) and η was calculated according to Eq. (1):

$$\eta = \frac{hS(T_{\text{max}} - T_{\text{surr}}) - Q_0}{I(1 - 10^{-A_{808}})} \tag{1}$$

where h is the heat transfer coefficient, S is the sample container surface area, $T_{\rm max}$ is the steady state maximum temperature, $T_{\rm surr}$ is the ambient room temperature, Q_0 is the baseline energy input by the solvent and sample container without the PDA@Au-HAp, I is the laser power, and A_{808} is the absorbance of PDA@Au-HAp at 808 nm. The value of hS was calculated by Eq. (2):

$$\tau_{\rm s} = \frac{m_d C_d}{h \rm S} \tag{2}$$

where τ_s is the characteristic thermal time constant, m_d is the mass of the PDA@Au-HAp solution (m_d) in g, and its heat capacity (C_d) is approximated to be 4.2 J g^{-1} k^{-1} (heat capacity of water). The heat energy (Q_0) of the sample container and solvent without PDA@Au-HAp were measured independently by Eq. (3):

$$Q_0 = hS(T_{\text{max}} - T_{\text{surr}})$$

(3)

The time constant was τ_s = 176.22 s based on the linear fit of the cooling period after 600 s vs. $-\ln\theta$. Accordingly, the photothermal

2.8. Antibacterial experiments

Staphylococcus aureus (S. aureus) and Escherichia coli (E. coli) on the solid Luria-Bertani (LB) agar plate were transferred to 20 mL of liquid LB culture medium and grown at 37 °C for 12 h under 180 rpm rotation. 500 μL of the diluted bacterial suspension (10 7 CFU/mL) were incubated with the LB culture medium containing PBS (control), H₂O₂, Au-HAp, PDA@Au-HAp, Au-HAp + H₂O₂, PDA@Au-HAp + H₂O₂. Another group was processed under the same conditions with NIR irradiation (808 nm, 1.0 W cm $^{-2}$) for 10 min. The final concentrations of Au-HAp or PDA@Au-HAp, H₂O₂, and bacteria were 200 $\mu g/mL$ 100 mM, and 1.0 \times 10 5 CFU mL $^{-1}$. After incubation for 10 min, the solution was placed on a solid medium by the spread plate method and cultured for 24 h before counting the number of the bacterial colonies. The control experiments were performed in parallel.

conversion efficiency calculated by Eqs. (3) and (1) was η = 13.28%.

$$Antibacterial \ rate(\%) \ = \left(1 - \frac{CFU_{experimental \ group}}{CFU_{control \ group}}\right) \times 100\%$$

After treatment with Au-HAp, PDA@Au-HAp and H_2O_2 for 8 h, the *S. aureus* and *E. coli* bacteria were harvested by centrifugation and washed with PBS. The bacteria were stained with PI (Propidium Iodide) and SYTO9 (LIVE/DEAD Backlight Bacterial Viability Kit) for 15 min and washed twice with PBS. The live and dead bacteria were then observed by fluorescence microscopy (IFM, Olympus, IX73).

2.9. Bacteria morphology

After the antibacterial tests, the bacterial suspension was drained completely and the adherent *S. aureus* and *E. coli* on the bottom of the 48-well plate were fixed with 2.5% glutaraldehyde for 2 h, dehydrated with alcohol of different concentrations of 30%, 50%, 70%, 90%, and 100% successively for 15 min, and dried in air prior to SEM observation.

2.10. Cell culture

The NIH3T3 cells were used to evaluate the cytotoxicity. The cells were cultured in 1% penicillin–streptomycin solution (HyClone) and MEM/EBSS (HyClone) supplemented with 10% fetal bovine serum (FBS) in a humidified atmosphere of 5% $\rm CO_2$ at 37 °C. The cell culture medium was refreshed every three days.

2.11. Cell viability

The *in vitro* cytotoxicity was measured using a 3-(4,5-dimethyl thiazol-2-yl)-2,5-diphenyltetrazolium bromide (MTT) assay of cellular activity on the NIH3T3 cells. The NIH3T3 cells (200 μL total volume per well) were seeded on 96-well plates and after incubation for 24 h, the samples were added and incubated for 24 h. To determine the toxicity, the MTT solution with a concentration of 5 $\mu g/mL$ was added into each well and incubated for 4 h at 37 °C. The medium was discarded and a dimethyl sulfoxide (DMSO) solution (200 μL) was added to each well. The plate was shaken for 10 min and the supernatant fluid was taken out to measure the optical density (OD) on a SpectraMax i3 Platform (Molecular Devices, California, USA) at a wavelength of 490 nm. The results were expressed as the percentage of cell viability and all the measurements were carried out in triplicate.

2.12. In vitro cell morphology and migration assay

The cells with a density of 1×10^4 cell/ml were cultured on 48-well plates for 24 h and rinsed three times with PBS (pH = 7.4). 4% formaldehyde was added to fix the cells at room temperature for 10 min. The cells were stained with FITC (YiSen, Shanghai) at room temperature for 30 min after rinsing with PBS (pH = 7.4) three times. Subsequently, the cells were stained with DAPI (YiSen, Shanghai) for 30 s. An inverted fluorescence microscope (IFM, Olympus, IX73) was used to observe the cell morphology.

In the cell migration assay, an *in vitro* scratch assay was conducted as previously reported. The cells were seeded on 6-well plates and cultured in the cell culture medium for 24 h to produce a confluent monolayer. A vertical scratch was created with a P1000 pipette tip. Each well was washed with 1 mL of the medium to remove ell debris and smooth the scratch edge. 2 mL of the medium were added to each well and the concentration of HAp, Au-HAp, and PDA@Au-HAp was 200 µg/mL. After 24 h, the cells were examined for the morphology and photographed by a fluorescence microscope (IFM, Olympus, IX73). The relative wound area (%) = A/A₀ × 100%, where the initial wound area (A₀) and wound area after 24 h incubation (A) were determined using the ImageJ software.

2.13. Quantitative real-time polymerase chain reaction (qRT-PCR)

The total RNA was extracted using Total RNA Kit I (50) (OMEGA) and quantified on the NanoDrop 2000 spectrophotometer (Thermo Scientific). The RNA samples (500 ng each) were reversely transcribed to cDNA using a PrimeScript RT Master Mix (TaKaRa, Japan) according to the manufactures' instructions. qRT-PCR was performed on a BIO-RAD CFX96 touch q-PCR system (CFX96, BIO-RAD) using SYBR Premix Ex TaqTM II (TliRNaseH Plus) (Takara). The gene expression of bFGF, COL I, and COL III was analyzed and the gene expression level of GADPH was used for normalization. Quantification of the gene expressions was based on the comparative cycle-threshold method.

2.14. In vivo mice wound model and healing process

All the experimental protocols were approved by Hubei Provincial Centers for Disease Prevention & Control and the male Sprague-Dawley rats (2 months old; 250 ± 12 g) were obtained from Wuhan Centers for Disease Prevention & Control. The rats were individually raised in cages at a standardized temperature for 2 days and evenly divided into four groups with three rats in each group: PBS + NIR (control group, group I), H₂O₂ + NIR (group II), PDA@Au-HAp + NIR (group III), PDA@Au-HAp + H₂O₂ + NIR (group IV). Prior to surgery, anesthesia was administered intraperitoneally with 3% pentobarbital sodium solution (Sigma) at a dosage of 1.0 mL/kg. A wound of d = 6 mm (\sim 28 mm²) was made surgically on the right and left sides of the backbone. The wounds were infected with the bacterial suspension of 10 μ L S. aureus with 1 \times 10 9 CFU mL $^{-1}$ and then 5 μ L of $200 \ \mu g \ mL^{-1}$ of PDA@Au-HAp and $100 \ \mu M \ H_2O_2$ solutions were dropped onto the wound area of the corresponding groups. After 10 min (for NIR treated groups), the wound area was irradiated with an 808 nm NIR laser (power density: 1 W cm⁻²) for 10 min. The other four groups including PBS (control group), HAp, Au-HAp. PDA@Au-HAp were treated under the same conditions without NIR irradiation and bacterial suspension. A homemade Band-Aid consisting of sterile cotton covering the wound was changed at 24 h intervals. The wounds were photographed after 2, 5, and 10 days. To monitor the antibacterial activity in vivo, the samples in each group were collected from the wound area using a sterile swab and they were placed in 5 mL of the LB broth and shaken for 8 h at 37 °C. 20 μL of the bacterial suspension of the culture solution were collected and spread on the LB agar plate and incubated at 37 °C for 24 h to form viable colony units. Finally, 1 mL of whole blood was collected from the rat for routine analysis on a veterinary automatic blood cell analyzer (Mindray BC-2800 Vet). The skin tissues were fixed with 10% formaldehyde before the histology analysis. Hematoxylin and eosin (H&E) staining was performed in the histological analysis and Masson's trichrome staining was employed for collagen formation assessment.

2.15. Statistical analysis

All the data are evaluated as mean ± standard deviation based on at least three tests and contrasted with Kruskal – Wallis oneway analysis of variance (ANOVA).

3. Results and discussion

3.1. Synthesis and characterization of polydopamine-assisted Auhydroxyapatite nanoparticles

The schematic of the synthesis of PDA@Au-HAp is shown in Fig. 2a. As shown in the TEM images (Fig. 2b), the average length

of the HAp nanorods varies from 80 to 100 nm and the transverse dimensions of the nanorods are 20-30 nm. After hydrothermal treatment with HAuCl₄ (precursor of Au NPs), the Au NPs are homogeneously distributed in the HAp nanorods and the average size is 4.9 ± 0.9 nm (Fig. 2c) according to the statistical analysis of 200 AuNPs by TEM. Further covering of PDA does not change the shape of the Au-HAp nanorods significantly (Fig. 2d), but the transverse dimension increases slightly. The high-resolution image shows that the thickness of the polymer coating is about 15 nm. The interplanar spacing between 0.28 nm and 0.34 nm represents the (2 1 1) and (0 0 2) planes of hydroxyapatite and the Au NPs are loaded along the direction of (220) with an interplanar distance of 0.14 nm (Fig. 2e) [36,37]. The EDS maps disclose homogeneous distributions of Ca, P, and Au in the PDA@Au-HAp NPs (Fig. S1). The XRD patterns are shown in Fig. 2f. The diffraction peaks from the (002), (211), (112), and (300) planes correspond to the expected peaks of HAp (ICPDS: 09-0432) [38]. As shown in Fig. 2g, the absorption peaks at 563 cm⁻¹ and 602 cm⁻¹ in the FTIR spectra of the precipitated samples can be assigned to P-O bending of the phosphate group resulting from -PO₄ in HAp, and those at 1620 cm⁻¹ and 1550 cm⁻¹ stem from amide I and amide II, indicating strong adhesion between HAp and PDA coating

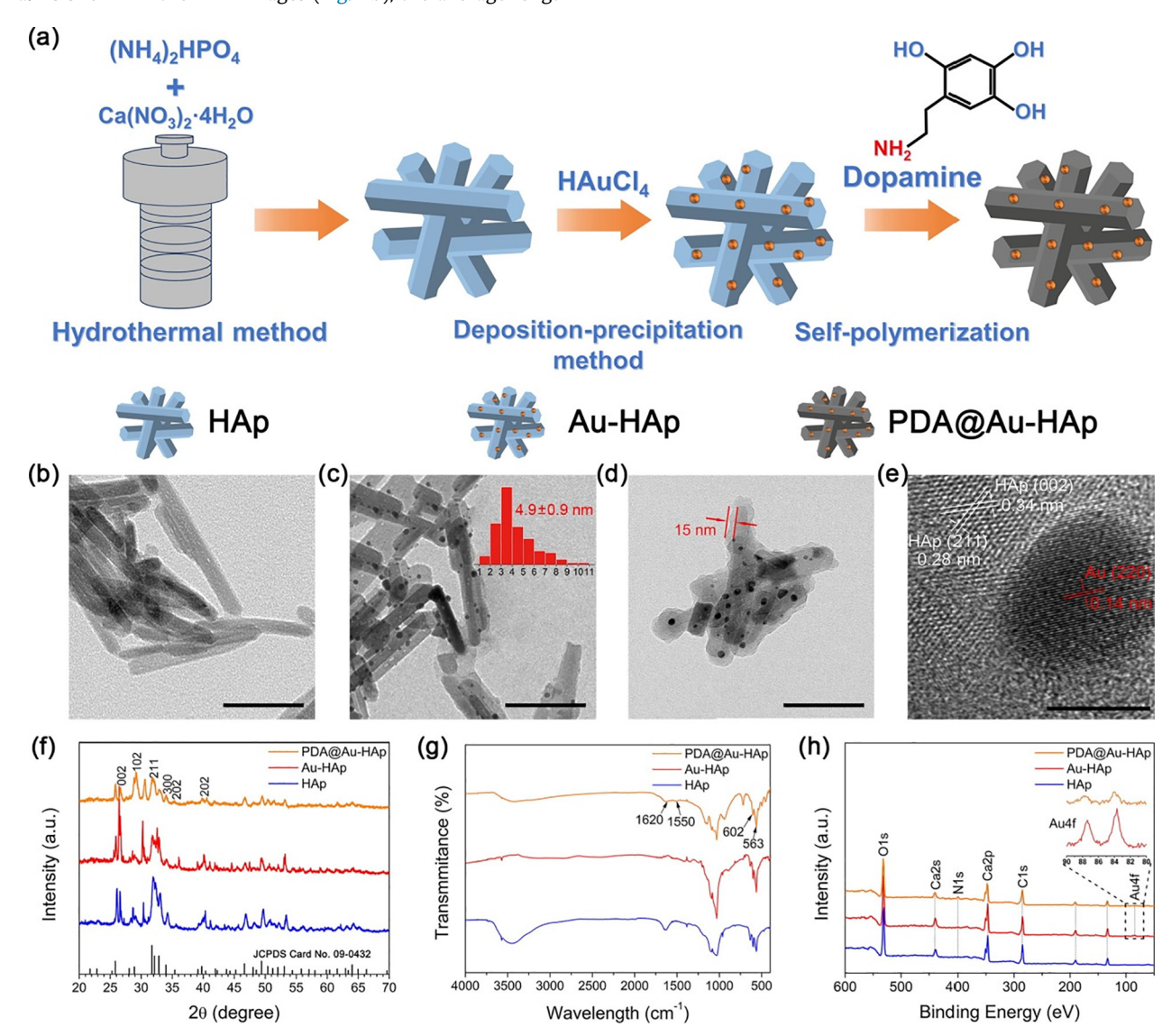


Fig. 2. (a) Schematic illustration of the synthesis of PDA@Au-HAp by loading Au NPs and the modification of PDA on hydroxyapatite synthesized by hydrothermal method. TEM images of (b) HAp, (c) Au-HAp, (d) PDA@Au-HAp and corresponding size distribution of Au NPs of PDA@Au-HAp (scale bar = 100 nm); (e) HR-TEM image of PDA@Au-HAp (scale bar = 5 nm); (f) XRD, (g) FT-IR and (h) XPS analysis of HAp, Au-HAp and PDA@Au-HAp.

[39,40]. As shown in Fig. 2h, the N 1s signal is observed from PDA@Au-HAp and the intensity of the O 1s peak increases, indicating successful coating of PDA. Au-HAp shows the Au 4f signal, but it is almost not detected due to the covering by PDA. Fig. S2a shows the C 1s XPS spectra of PDA@Au-HAp. The C—C peak at a binding energy of 284.8 eV and C—N peak at a binding energy of about 285.6 eV confirm the presence of the PDA coating [41]. The fitted peaks at 399.1, 400, and 400.6 eV correspond to C—N, C—N and C—NH₃⁺ in PDA, respectively (Fig. S2b) [42]. The peaks at 531.5 and 532.8 eV represent O—C and C—OH in PDA (Fig. S2c), respectively, further corroborating successful grafting of PDA on the surface of Au-HAp [43].

Supplementary data associated with this article can be found, in the online version, at https://doi.org/10.1016/j.actbio.2018.07.030.

3.2. Peroxidase-like activity and photothermal properties

The peroxidase-like activity of Au-HAp and PDA@Au-HAp is evaluated in the catalysis of peroxidase substrates 3. 3' 5. 5'tetramethylbenzidine (TMB) [44]. Both Au-HAp and PDA@Au-HAp catalyze oxidation of TMB in the presence of H_2O_2 (100 μ M) and produce a blue color after reacting for 10 min (Fig. 3a). The inset picture shows the photographs of the reaction system H₂O₂ + TMB, Au-HAp + H_2O_2 + TMB and PDA@Au-HAp + H_2O_2 + TMB from left to right. Au-HAp + H₂O₂ + TMB shows a deeper color than PDA@Au-HAp + H_2O_2 + TMB, indicating that the former has better catalytic ability due to the hindrance of PDA between the Au NPs and catalytic system. As shown in Fig. 3b, the relative catalytic activity rises gradually with temperature and like other nanomaterial-based peroxidase mimics [45], the maximum temperature of Au-HAp under irradiation is 43 °C and so we cannot get data at over 45 °C. The activity of Au-HAp and PDA@Au-HAp depends on the concentration of H2O2 (Fig. S3a) and pH (Fig. S3b). Even at a pH of 3.0, the peroxidase-like activity of PDA@Au-HAp remains at about 30% compared to that at pH of 7.0, revealing high catalytic activity in the physiological pH range of 5.0-7.4. The catalytic activity of Au-HAp and PDA@Au-HAp in the presence of a small concentration of H_2O_2 (100 μ M) is verified by oxidation of terephthalic acid (TA) which reacts with .OH to form 2-hydroxyl terephthalic acid (TAOH) and exhibits fluorescence at 435 nm [46]. Fig. 3c shows the fluorescence change in the solution of Au-HAp, PDA@Au-HAp, TA, and H₂O₂. After reacting for 12 h, fluorescence at 435 nm increases indicating the presence of .OH radicals. TA + Au-HAp + H₂O₂ and TA + PDA@Au-HAp + H₂O₂ exhibit obvious fluorescence at a pH of 7.4. As shown in Fig. 3d, the absorption peak at 548 nm observed from Au-HAp and PDA@Au-HAp indicates AuNPs. PDA@Au-HAp shows broad absorption compared to pure HAp and Au-HAp, especially in the near infrared (NIR) region. It has been reported that the π - π * transition of the polymeric backbone of the benzenoid ring contributes to the broad absorption, especially near the NIR region [47]. The inset picture shows color changes in the different samples. In comparison with the milky white solution, the color of Au-HAp suspension becomes light red and that of the PDA@ Au-HAp suspension is dark brown due to modification of PDA. The photothermal behavior of these samples in PBS solutions is examined by excitation with the 808 nm NIR (1 W cm⁻²). As shown in Fig. 3e and f, at 200 μ g/mL, the temperature of the PDA@Au-HAp PBS solution increases from 25.2 to 43.2 °C after irradiation for 10 min. In comparison, the temperature of pure PBS increases by only 0.5 °C and that of Au-HAp increases from 25.1 to 34.7 °C. As shown in Fig. S4, the photothermal conversion efficiency of PDA@Au-HAp is calculated to be 13.28% using the method developed by Roper et al [48]. Meanwhile, the temperature change of PDA@Au-HAp at different laser power is shown in Fig. S5.

3.3. In vitro antibacterial evaluation

As shown in Fig. 4a and b, a reduced bacteria population is observed from PDA@Au-HAp + H₂O₂. The number of bacterial colo-

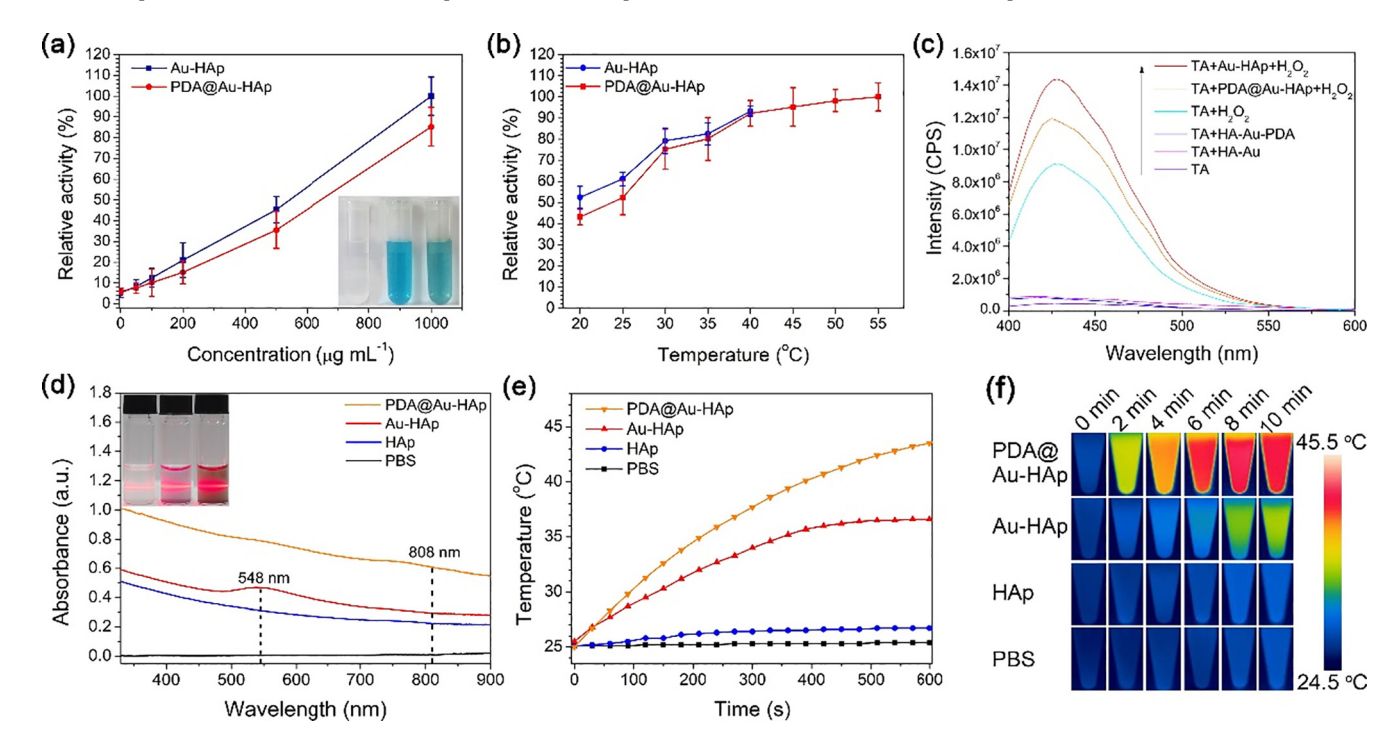


Fig. 3. Relative catalytic activity of Au-HAp and PDA@Au-HAp after incubation for 10 min towards (a) different concentration and (b) different temperature under 808 nm irradiation. Inset shows the photograph of the reaction system $H_2O_2 + TMB$, Au-HAp + $H_2O_2 + TMB$, and PDA@Au-HAp + $H_2O_2 + TMB$ from left to right (1 mM TMB, 200 μg/mL samples and 100 μM H_2O_2). (c) Formation of hydroxyl radical (.0H) determined at pH = 7.4 with TA as a fluorescent probe. Reaction conditions: 200 μg/mL samples, 100 μM H_2O_2 , 0.5 mM TA, PBS (pH = 7.4) incubated for 12 h at 37 °C under dark conditions. (d) UV-vis-NIR absorption and digital images of HAp, Au-HAp, and PDA@Au-HAp dispersed in PBS. (e) Temperature changes and corresponding (f) Infrared thermography of HAp, PDA@HAp, Au-HAp, and PDA@Au-HAp irradiated by the 808 nm laser.

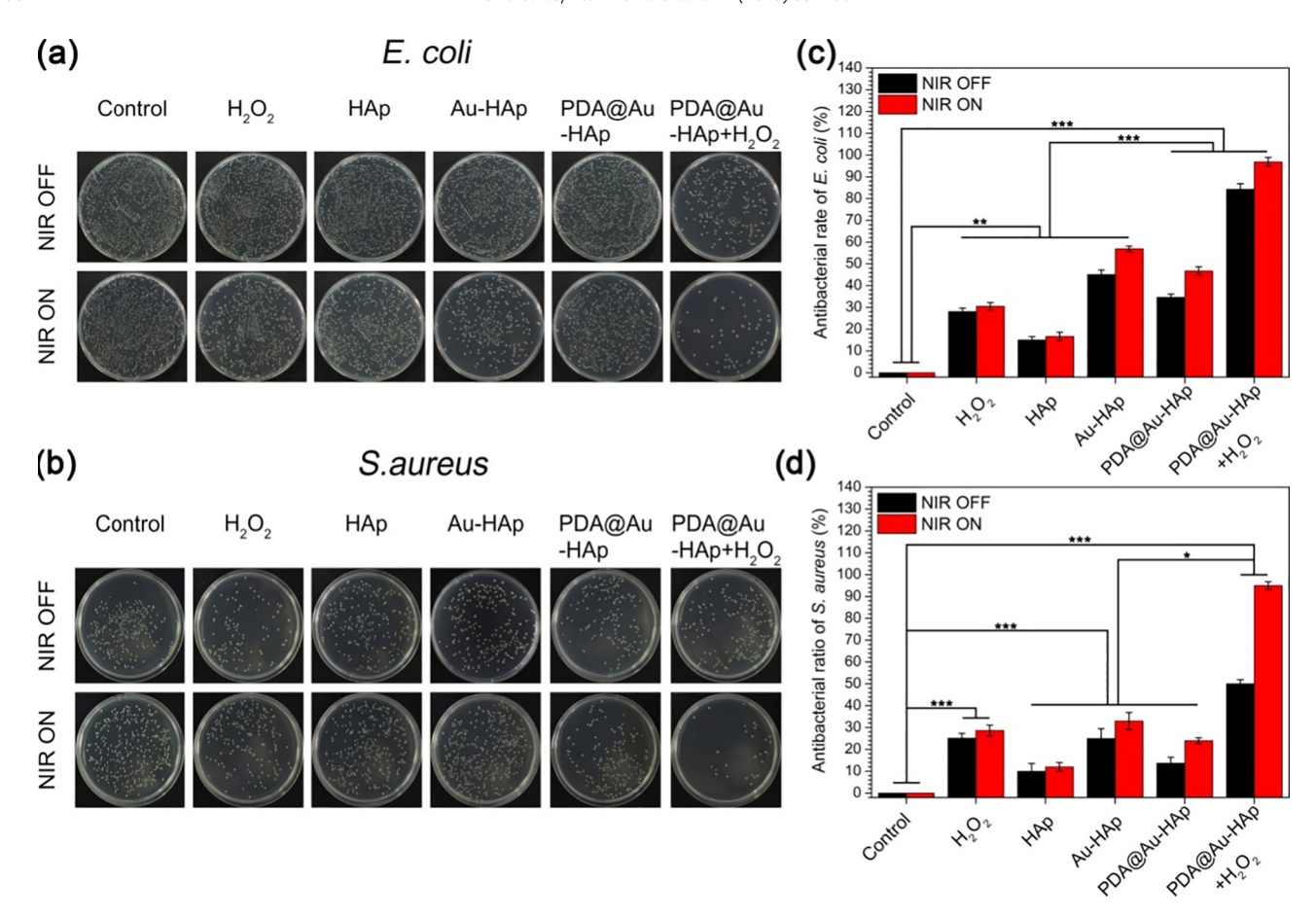


Fig. 4. Photographs of bacteria colonies formed by (a) *E. coli* and (b) *S. aureus* after exposure to Control (PBS), H_2O_2 , HAp, Au-HAp, PDA@Au-HAp, and PDA@Au-HAp + H_2O_2 after 20 min with or without 808 nm irradiation. Concentration: Au-HAp and PDA@Au-HAp: 200 μ g/mL, H_2O_2 : 100 μ M. The corresponding antibacterial rates of (c) *E. coli* and (d) *S. aureus* obtained from the spread plate results are presented as the mean \pm standard deviations: $^*P < 0.05$, $^*P < 0.01$ and $^{***}P < 0.001$, n = 3.

nies on PDA@Au-HAp is slightly less than that of the control group and that on Au-HAp is even less. A slightly decreased number of colonies is observed from the $\rm H_2O_2$ group, and HAp shows poor antimicrobial characteristics. After exposure to 808 nm NIR for 10 min, the bacterial colonies decrease in large number on PDA@Au-HAp + $\rm H_2O_2$, but those on PDA@Au-HAp decrease slightly. Because of the photothermal effect, the quantity of bacteria on Au-HAp also decreases and there are differences among the control, $\rm H_2O_2$, and HAp.

As shown in Fig. 4c and d, after culturing without light for 20 min, the antibacterial ratios of PDA@Au-HAp against E. coli and S. aureus are 34.6% and 13.7%, respectively, compared to 45.8% and 25.1% on pure Au-HAp. It is probably due to covering by PDA which hinders contact with bacteria and reduces the toxicity of the Au NPs. However, in the presence of 100 µM H₂O₂, the ratios on PDA@Au-HAp + H₂O₂ group against E. coli and S. aureus are 84.2% and 50.2%, respectively, suggesting that PDA@Au-HAp catalyzes decomposition of H₂O₂ to produce .OH to improve the bacterial resistance. Meanwhile, owing to the small H₂O₂ concentration, the H₂O₂ group only shows weak antibacterial characteristics and HAp itself has no obvious antibacterial activity [49,50]. The concentration dependent antibacterial results are shown in Fig. S6. Fig. S6a and S6b show that a large concentration of H₂O₂ (above 10^{-2}) kills E. coli and S. aureus effectively because of .OH, but PDA @Au-HAp exhibits negligible antibacterial effects towards E. coli and S. aureus (54.1% and 20.5%) even at the concentration of 1 mg/mL (Fig. S6c and S6d). The results show that peroxidase catalysis alone cannot produce the ideal bactericidal effects.

When the bacteria are incubated with PDA@Au-HAp + H_2O_2 for 10 min and then irradiated with 808 nm NIR for 10 min (Fig. 4c-d),

the antibacterial rates increase to 96.8% and 95.2% for *E. coli* and *S. aureus* thus suggesting some synergy of the photothermal and catalytic effects. Nevertheless, PDA@Au-HAp only shows 46.3% and 23.2% antibacterial effects against *E. coli* and *S. aureus* under NIR irradiation and so a temperature of 45.2 °C is not enough to kill the majority of the bacteria. The antibacterial effects of Au-HAp improve slightly because of the weak photothermal effect. The results show that *S. aureus* is more tolerant to temperature than *E. coli*. It is possibly because the Gram-positive *S. aureus* possesses a thick peptidoglycan layer (20–80 nm) which consists of amino acids, surface proteins, teichoic acids, and lipoids, whereas the Gram-positive bacteria *E. coli* lacks the outer membrane thus becoming more prone to external interactions through a the peptidoglycan layer [51].

The morphology and membrane integrity of the bacteria before and after the different treatments are examined by SEM. As shown in Fig. 5a and b, clear edges and smooth and intact cell walls are observed from the control group. After culturing with H2O2 or PDA@Au-HAp for 20 min, a few disruptions occur on the cell walls indicating that H₂O₂ or PDA@Au-HAp alone has little toxicity against E. coli. PDA@HAp and Au-HAp show almost no antibacterial activity even with NIR irradiation (Fig. 5a). However, after light exposure of PDA@Au-HAp + H₂O₂ for 20 min, the red arrow in the figure shows that the bacterial surface becomes rough and wrinkled because the generated .OH oxidizes lipids and damages the cell membrane. After treatment with PDA@Au-HAp + H₂O₂ for 10 min and irradiation for another 10 min, the E. coli cells lose the cellular integrity completely as manifested by outflow of the cell matrix indicative of stronger antibacterial activity. As shown in Fig. 5b, the results for S. aureus are similar to those of E. coli. In

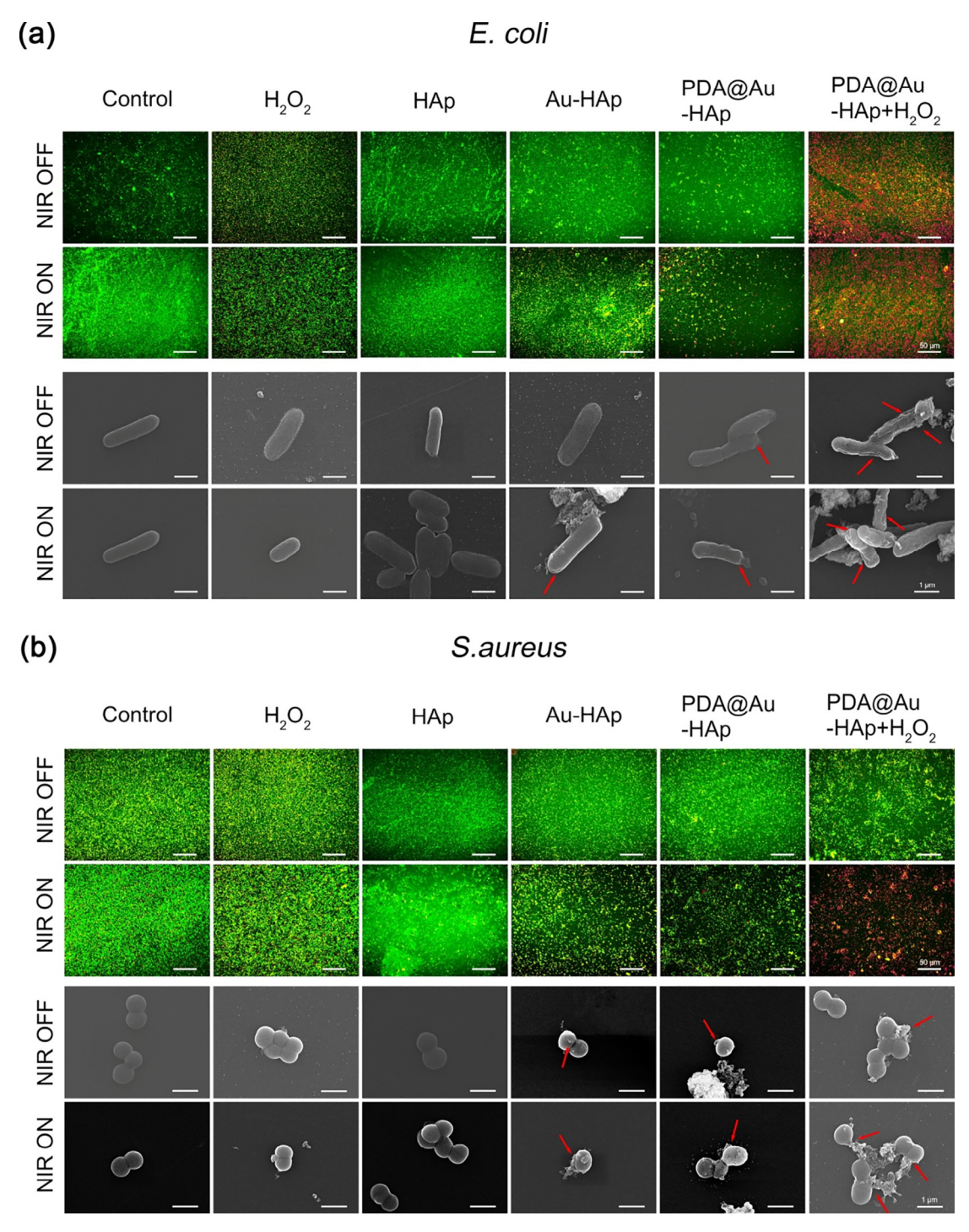


Fig. 5. Typical fluorescence images (scale bar is 50 μ m) and SEM images (scale bar is 1 μ m) of (a) *E. coli* and (b) *S. aureus* by various treatments. Green and red stains signify viable and dead bacteria and red arrows represent damage of cell membranes. (For interpretation of the references to color in this figure legend, the reader is referred to the web version of this article.)

the control group, the *S. aureus* cells are spherical and smooth but in the presence of PDA@Au-HAp or H_2O_2 , the membranes are damaged. The cell walls are rough and damaged after light irradiation and incubation with PDA@Au-HAp + H_2O_2 for 10 min. The results are consistent with those observed by optical spectroscopy. The antibacterial ability is also assessed by LIVE (green)/DEAD (red) kit fluorescent microscopy. Fig. 5a and b show that almost all the *E. coli* and *S. aureus* cells are viable after treated with Au-HAp and PDA@Au-HAp even with irradiation. In the presence of H_2O_2 , only small red fluorescent signals are detected but after mixing

PDA@Au-HAp with H₂O₂, the red spots increase, indicating better bactericidal effects. The results demonstrate efficient controlled-temperature PTT in the presence of a small concentration of H₂O₂.

3.4. In vitro wound healing evaluation

An *in vitro* scratch assay is conducted to determine the effects of PDA@Au-HAp samples on skin cell migration [52]. The NIH3T3 cells have a similar wound width after scratching with a pipet tip (Fig. 6a). The cells move toward the wound area and the scratch

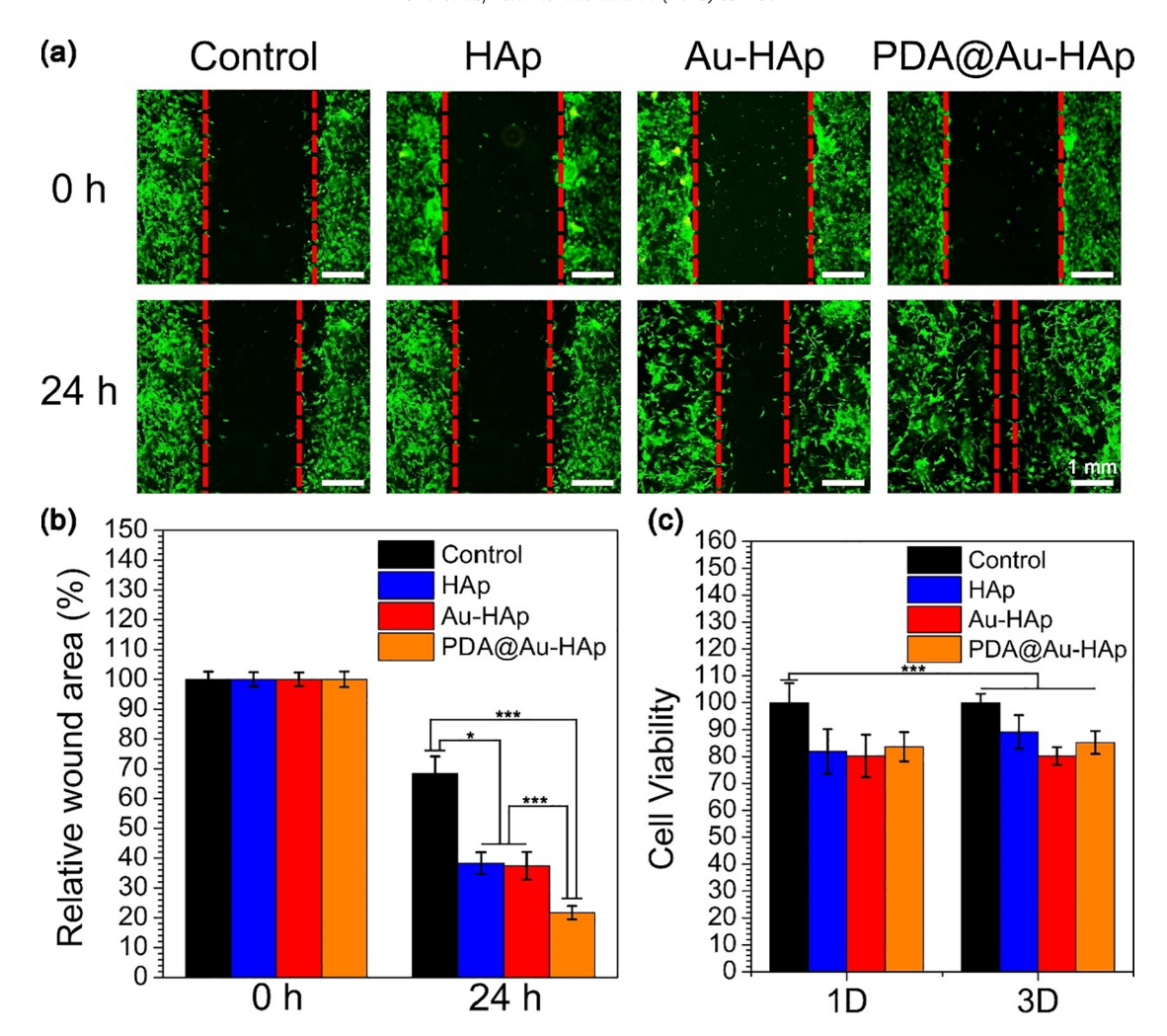


Fig. 6. (a) *In vitro* scratch assay of NIH3T3 cells cultured under different conditions. (b) Quantification of the relative wound area after 24 h. (c) Relative viabilities of NIH3T3 cells incubated with Control (PBS), HAp, Au-HAp and PDA@Au-HAp for 1 day and 3 days. Data were presented as the mean ± standard deviations: *P < 0.05, **P < 0.01 and ***P < 0.001, n = 3.

almost disappears from PDA@Au-HAp after 24 h. The wound area (Fig. 6b) decreases to 20.1% for PDA@Au-HAp compared to the control group (68.4%). HAp and Au-HAp show decreases of 38.4% and 37.3%, respectively, possibly because PDA benefits cell growth and adhesion [53]. The scratch assay indicates that PDA@Au-HAp promotes migration of NIH3T3 cells. As shown in Fig. 7c, the control (PBS), HAp, Au-HAp, and PDA@Au-HAp show reduced cell viability

compared to the control after incubation for 1 and 3 days. The cytotoxicity of PDA@Au-HAp depends on the concentration (Fig. S7a). At 1000 μ g/mL, more than 70% of the cells still survive. In addition, Fig. S7b shows that H_2O_2 at a concentration below 10^{-4} M has less influence on the NIH3T3 cells. When H_2O_2 is mixed with PDA@Au-HAp, the cell viability decreases rapidly but recovers three days later (Fig. S8).

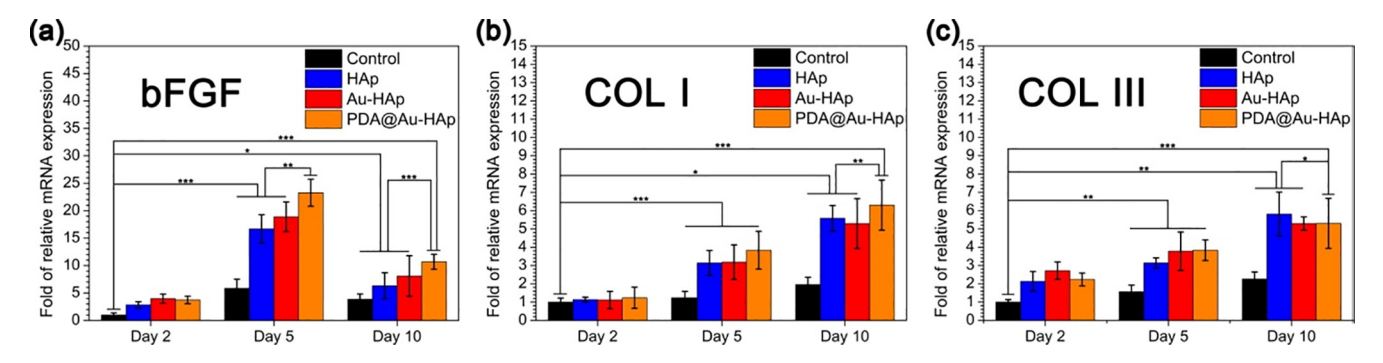


Fig. 7. Wound healing-related gene expressions of (a) bFGF, (b) COL I and, (c) COL III with treatment of Control (PBS), HAp, Au-HAp, and PDA@Au-HAp. The data are generated by real-time PCR and presented as relative to control cells cultured in PBS at day 2 by using normalization against a GAPDH reference. The data are presented as the mean \pm standard deviations: $^*P < 0.05$, $^*P < 0.01$ and $^{***}P < 0.001$, n = 3. (Concentration: HAp, Au-HAp, and PDA@Au-HAp: 200 μ g/mL).

To further investigate the process of wound healing, the gene expression of the basic fibroblast growth factor (bFGF), type I collagen (Col I), and type III collagen (Col III) for NIH3T3 fibroblasts are analyzed by the quantitative reverse transcription polymerase chain reaction (qRT-PCR). Fig. 7a shows that for HAp, Au-HAp, and PDA@Au-HAp, the mRNA expressions of bFGF are higher than that of the control on the 5th and 10th day and reduced bFGF mRNA expression is observed on the 10th day. This provides evidence about extracellular matrix (ECM) reorganization and release of growth factors during this period [54]. PDA@Au-HAp shows the highest mRNA level because PDA promotes cell adhesion and migration. The cells cultured with HAp, Au-HAp, and PDA@Au-HAp show higher mRNA levels of COL I and COL III throughout the observation period than the control group (Fig. 7b-c), further suggesting that the hydroxyapatite-based materials enhance production of collagen fibers during healing. The enhanced gene expressions of COL I and COL III reveal enhanced recombination of the collagen network of PDA@Au-HAp on the genetic level.

3.5. In vivo wound healing assessment

In the in vivo experiments, the mice with wounds are divided into four groups: PBS, HAp, Au-HAp, PDA@Au-HAp, Fig. 8a shows the optical images of the untreated wounds and those treated with HAp, Au-HAp, PDA@Au-HAp at time points of 0, 2, 5 and 10 days. The wounds for PDA@Au-HAp are obviously smaller (Fig. 8a). Compared to Au-HAp and PDA@Au-HAp, there are no significant differences after the 2-day and 5-day treatment. However, after the 10day treatment, the skin around the wound is still red and swollen for the Au-HAp group and PDA@Au-HAp shows dramatic therapeutic effects. The size of the wound illustrates the healing trend (Fig. 8b). H&E staining and Masson's trichrome staining are used to determine the structure of epidermis and formation of collagen fiber during wound healing. As shown in Fig. 9, after the 2-day treatment, loose and disordered connective tissues in the collagen fibers (black rectangles) are observed from both Au-HAp and PDA@Au-HAp. Dermal fibroblasts (green arrows) and newborn blood vessels (blue arrows) filled with a large number of red blood cells (cyan arrows) are observed from PDA@Au-HAp after the 5day treatment. Large amounts of connective tissues (red rectangles) are observed from PDA@Au-HAp after the 10-day treatment but only PDA@Au-HAp shows more organized collagen fibrils compared to Au-HAp, thus indicating the positive effects of PDA on the wound healing process.

Bacterial infection often occurs during wound healing. To evaluate the in vivo photothermal therapeutic effects, the real time disinfection and wound healing process are investigated with an animal model under NIR irradiation. The experiments are divided into four groups: (I) PBS + NIR (control), (II) H₂O₂ + NIR, (III) PDA@Au-HAp + NIR, and (IV) PDA@Au-HAp + H₂O₂ + NIR. The traumas are photographed on days 2, 5, and 10. The results are shown in Fig. 10. All the groups show severe bacterial infection with ichors after the 2-day treatment. As shown in Fig. 10a, recovery of group (III) and group (IV) is better than that of the control after the 5-day treatment, especially PDA@Au-HAp + H₂O₂ + NIR. Moreover, the wounds in group (I) and group (II) show exudation of tissue fluids, whereas group (III) begins to scab and group (IV) has no purulent fluids after the 5-day treatment. At the end of the 10-day treatment. the wounds of the control and H₂O₂ + NIR groups do not recover well, but those of PDA@Au-HAp and H₂O₂ exhibit productive healing. The size of the wounds also shows the healing trend (Fig. 10b).

Hematoxylin and eosin (H&E) staining of the epidermis of the repaired tissues are performed on days 2, 5, and 10. Fig. 11 shows that after the 2-day treatment, a large number of neutrophils (black arrows) are observed from all the groups, indicative of severe bacterial infection. The large amount of dead cell debris (red arrows) and loose and disordered connective tissues in the collagen fibers (black rectangles) are observed from the control and H_2O_2 + NIR groups. In the therapeutic process, both the control and H₂O₂ groups show some inflammatory cells, but new fibroblasts and blood vessels begin to emerge from the PDA@Au-HAp + NIR and PDA@Au-HAp + H₂O₂ + NIR groups. Regeneration and differentiation of fibroblasts under the dermis and regeneration of the skin around the wound are important processes in wound healing [55]. After the 10-day treatment, compared with the control group, the structure of the skin epidermis of group (III) and group (IV) is clear and complete. The collagen fiber is regenerated, but infected necrotic foci (blue rectangles) appear from the control and H_2O_2 + NIR groups, suggesting that the wounds have not yet healed. The amounts of adherent bacteria after the 2-day and 5day treatments are examined by Giemsa staining (red arrows in Fig. 11). Compared to the control and $H_2O_2 + NIR$ groups, the amount of bacteria of PDA@Au-HAp + H₂O₂ + NIR group decreases significantly, thereby verifying the antibacterial ability in vivo. Furthermore, besides larger amount of WBCs (Fig. S9a), the neutrophils in the whole blood of the rats collected from the treatment groups also show higher levels than those of the control group after the 2-day treatment (Fig. S9b). All in all, this synergistic antibacterial system not only kills bacteria effectively, but also promotes scar generation to protect the wounded tissues.

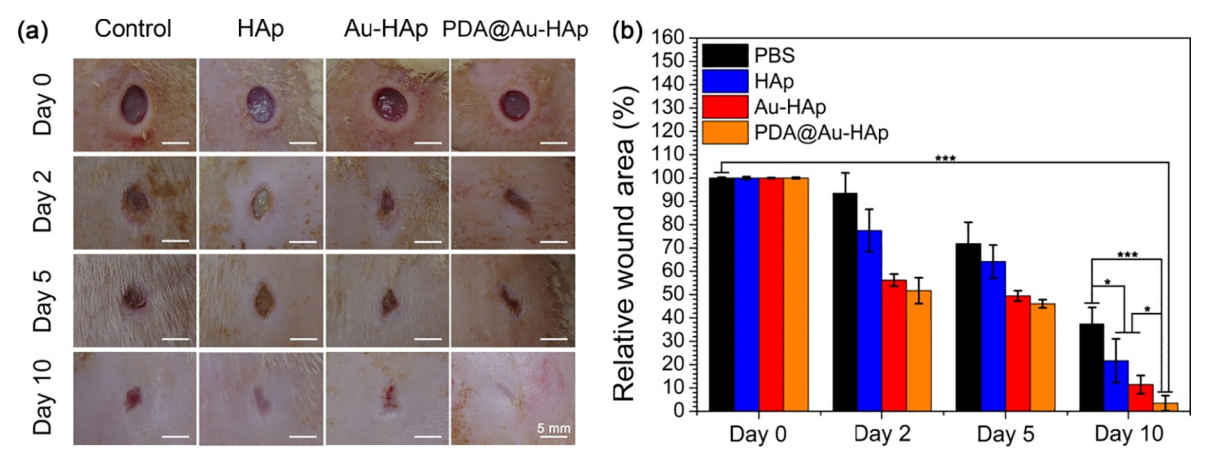


Fig. 8. (a) Representative skin wound photographs on days 0, 2, 5, and 10 (scale bar = 5 mm) and (b) Relative wound area of control (PBS), HAp, Au-HAp, and PDA@Au-HAp groups. The data are presented as the mean ± standard deviations: *P < 0.05, *P < 0.01 and ***P < 0.001, n = 3.

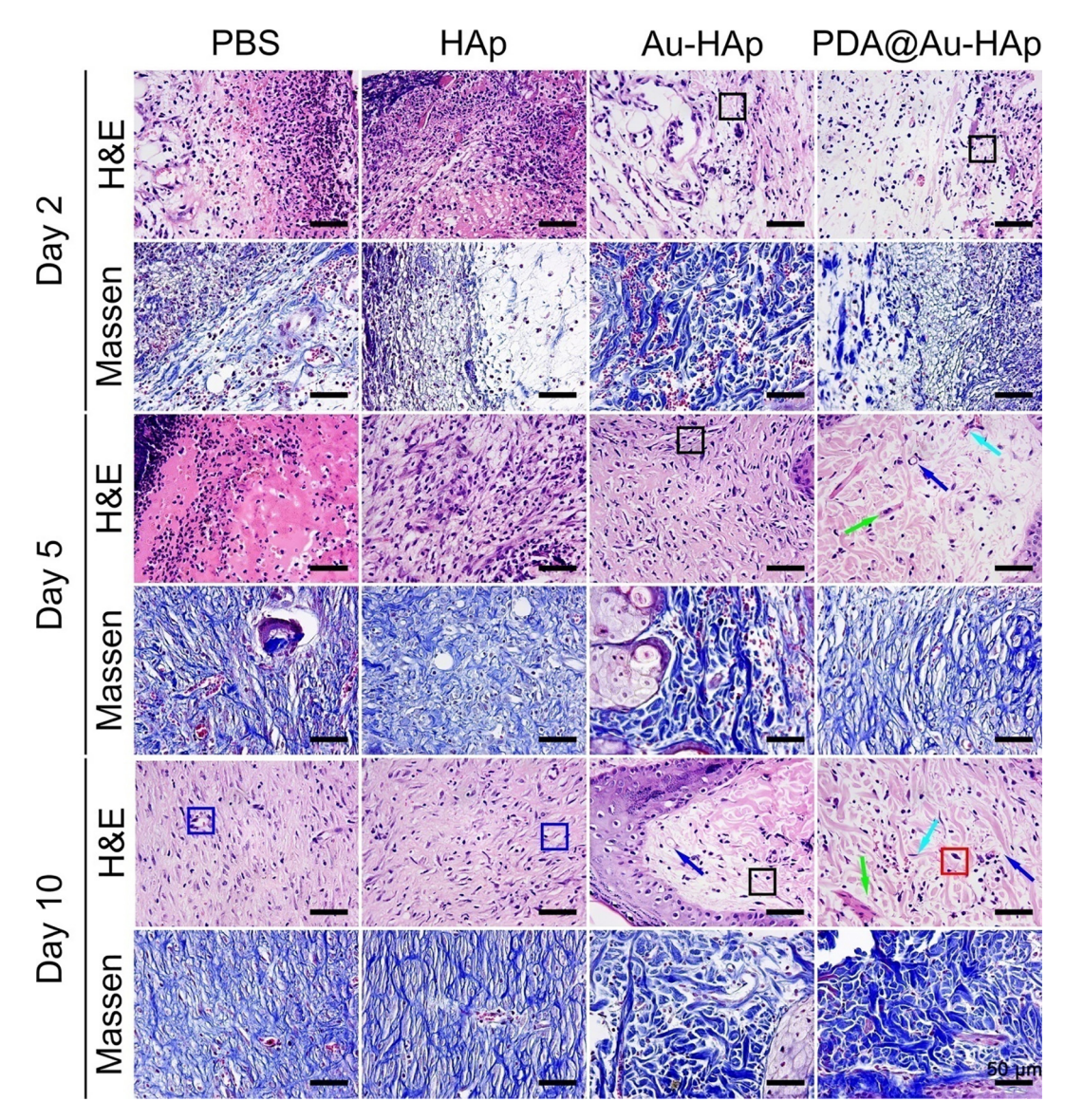


Fig. 9. H&E and Masson staining of wound tissues treated with control (PBS), HAp, Au-HAp, and PDA@Au-HAp on days 2, 5, and 10 (scale bar = 50 μm). Black rectangles, green arrows, blue arrows, cyan arrows, blue rectangles, and red rectangles represent disorder in the collagen fibers, dermal fibroblasts, newborn blood vessels, red blood cells, infected necrotic foci, and connective tissues, respectively. (For interpretation of the references to color in this figure legend, the reader is referred to the web version of this article.)

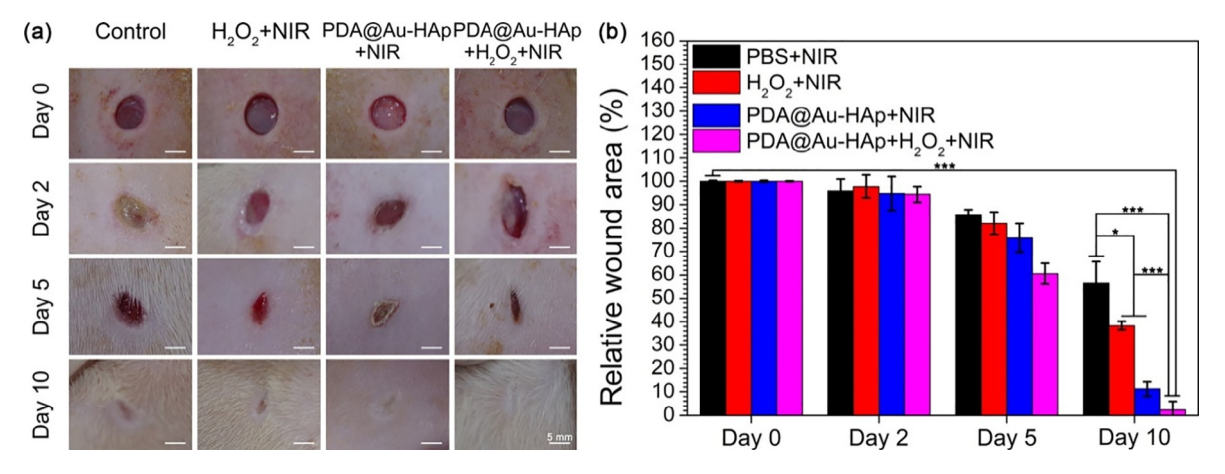


Fig. 10. Assessment of wound healing accompanied with bacterial infection (scale bar = 5 mm). (a) Representative skin wound photographs induced by *S. aureus* on days 0, 2, 5, and 10. (b) Relative wound area of control (PBS), $H_2O_2 + NIR$, PDA@Au-HAp + NIR, and $PDA@Au-HAp + H_2O_2 + NIR$ groups. The data are presented as the mean \pm standard deviations: $^*P < 0.05$, $^*P < 0.01$ and $^*P < 0.001$, n = 3.

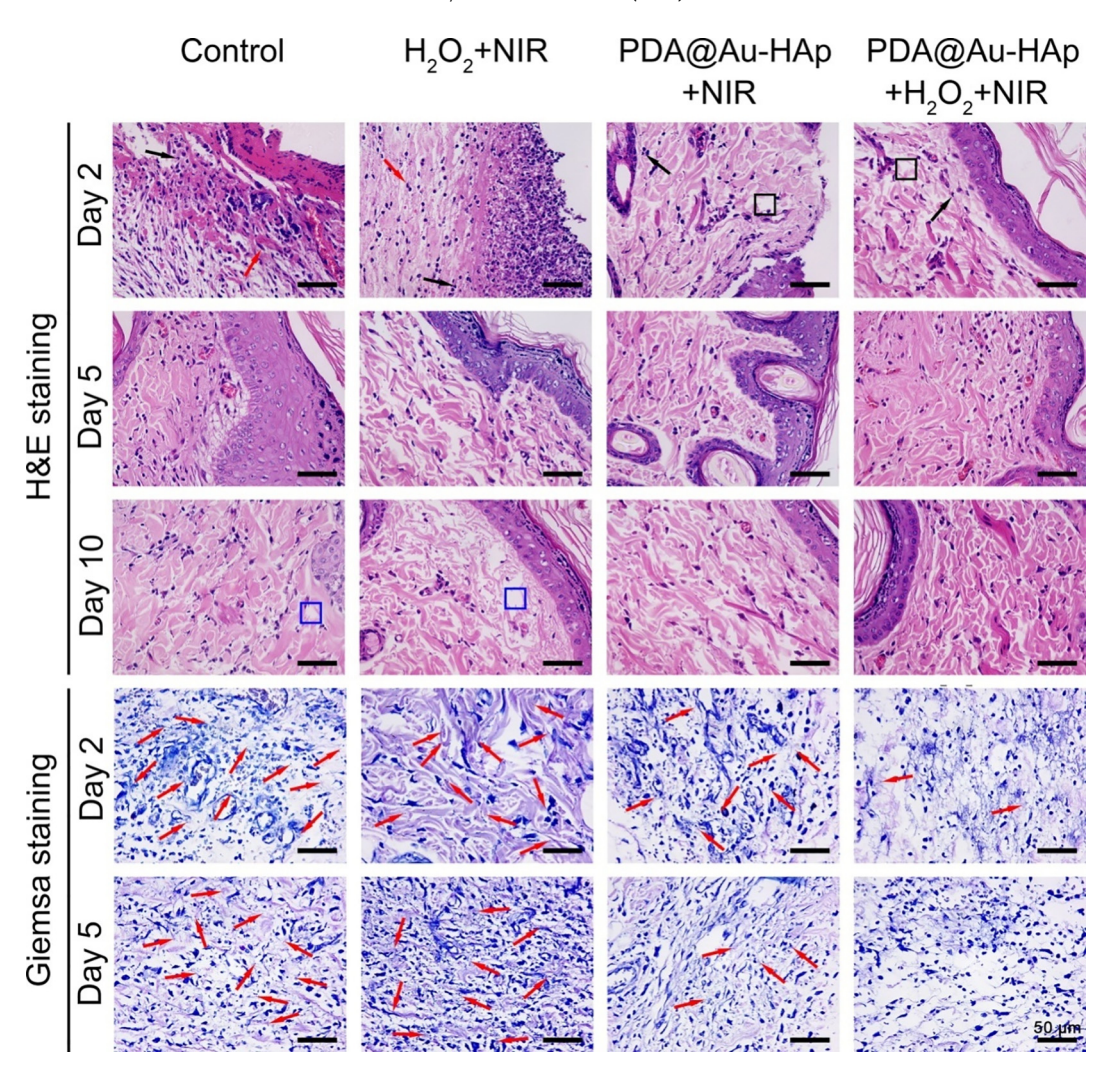


Fig. 11. H&E staining analysis of wound tissues treated with control (PBS), $H_2O_2 + NIR$, PDA@Au-HAp + NIR, and PDA@Au-HAp + $H_2O_2 + NIR$ on days 2, 5, and 10 and corresponding Giemsa staining on days 2 and 5. (scale bar = 50 μ m.)

4. Conclusion

A controlled-temperature photothermal antibacterial therapeutic platform comprising PDA-assistance and Au NPs loaded HAp nanorods is designed and demonstrated. The Au-loaded HAp nanorods show excellent peroxidase catalytic activity and PDA has remarkable photothermal conversion efficiency. By taking advantage of the peroxidase catalytic and photothermal capability, the materials can kill both E. coli (Gram-negative) and S. aureus (Gram-positive) with higher efficacy in a short time at a low photothermal temperature of 45 °C compared to the peroxidase catalytic process or separate photothermal therapy alone. The treatment thus avoids possible damage of normal tissues at a higher temperature. The PDA@Au-HAp promotes tissue reconstruction by improving the formation of granulation tissues and synthesis of collagens. The results reveal a safe, simple, effective, and rapid way to disinfect wound and expedite tissue regeneration and healing.

Acknowledgments

This work is jointly supported by the National Natural Science Foundation of China, 51671081, and 51422102, National Key Research and Development Program of China, no. 2016YFC1100600 (subproject 2016YFC1100604), Hong Kong

Research Grants Council (RGC) General Research Funds (RGC) General Research Funds (GRF) Nos. CityU 11301215 and 11205617, Hong Kong ITC (ITS/287/17, GHX/002/14SZ), Health and Medical Research Fund (03142446), as well as Hong Kong RGC GRF (17214516) and RGC/NSFC (N_HKU725-16).

References

- [1] B.R. Levin, R. Antia, Why we don't get sick: the within-host population dynamics of bacterial infections, Science 292 (2000) 1112–1116.
- [2] R.L. Gallo, L.V. Hooper, Epithelial antimicrobial defence of the skin and intestine, Nat. Rev. Immunol. 12 (2012) 503–516.
- [3] L.L. Ling, T. Schneider, A.J. Peoples, A.L. Spoering, I. Engels, B.P. Conlon, A. Mueller, T.F. Schäberle, D.E. Hughes, S. Epstein, M. Jones, L. Lazarides, V.A. Steadman, D.R. Cohen, C.R. Felix, K.A. Fetterman, W.P. Millett, A.G. Nitti, A.M. Zullo, C. Chen, A new antibiotic kills pathogens without detectable resistance, Nature 517 (2015) 455–459.
- [4] G.D. Mogosanu, A.M. Grumezescu, Natural and synthetic polymers for wounds and burns dressing, Int. J. Pharm. 463 (2014) 127–136.
- 5] M. Ul-Islam, T. Khan, W.A. Khattak, J.K. Park, Bacterial cellulose-MMTs nanoreinforced composite films: novel wound dressing material with antibacterial properties, Cellulose 20 (2013) 589–596.
- [6] M. Baym, T.D. Lieberman, E.D. Kelsic, R. Chait, R. Gross, I. Yelin, R. Kishony, Spatiotemporal microbial evolution on antibiotic landscapes, Science 353 (2016) 1147–1151.
- [7] M.A. Fischbach, C.T. Walsh, Antibiotics for emerging pathogens, Science 325 (2009) 1089–1093.
- [8] M.N. Alekshun, S.B. Levy, Molecular mechanisms of antibacterial multidrug resistance, Cell 128 (2007) 1037–1050.
- [9] S. Rahimi, Z.T. Zadeh, M.A.K. Torshizi, R. Omidbaigi, H. Rokni, Effect of the three herbal extracts on growth performance, immune system, blood factors and

- intestinal selected bacterial population in broiler chickens, J. Agr. Sci. Tech. 13 (2011) 527–539.
- [10] L. Tan, J. Li, X. Liu, Z. Cui, X. Yang, K.W.K. Yeung, H. Pan, Y. Zheng, X. Wang, S. Wu, *In situ* disinfection through photoinspired radical oxygen species storage and thermal-triggered release from black phosphorous with strengthened chemical stability, Small 14 (2018) 1–11.
- [11] C. Fasciani, M.J. Silvero, M.A. Anghel, G.A. Argüello, M.C. Becerra, J.C. Scaiano, Aspartame-stabilized gold-silver bimetallic biocompatible nanostructures with plasmonic photothermal properties, antibacterial activity, and longterm stability, J. Am. Chem. Soc. 136 (2014) 17394–17397.
- [12] M. Ji, M. Xu, W. Zhang, Z. Yang, L. Huang, J. Liu, Y. Zhang, L. Gu, Y. Yu, W. Hao, P. An, L. Zheng, H. Zhu, J. Zhang, Structurally well-defined Au@Cu2-xS core-shell nanocrystals for improved cancer treatment based on enhanced photothermal efficiency, Adv. Mater. 28 (2016) 3094–3101.
- [13] L. Xiao, J. Sun, L. Liu, R. Hu, H. Lu, C. Cheng, Y. Huang, S. Wang, J. Geng, Enhanced photothermal bactericidal activity of the reduced graphene oxide modified by cationic water-soluble conjugated polymer, ACS Appl. Mater. Interfaces 9 (2017) 5382–5391.
- [14] Y. Yang, W. Zhu, Z. Dong, Y. Chao, L. Xu, M. Chen, Z. Liu, 1D Coordination polymer nanofibers for low-temperature photothermal therapy, Adv. Mater. 29 (2017) 1–12.
- [15] D. Yoo, H. Jeong, S.H. Noh, J.H. Lee, J. Cheon, Magnetically triggered dual functional nanoparticles for resistance-free apoptotic hyperthermia, Angew. Chem. Int. Ed. 52 (2013) 13047–13051.
- [16] T. Zhou, Y. Zhu, X. Li, X. Liu, K.W.K. Yeung, S. Wu, X. Wang, Z. Cui, X. Yang, P.K. Chu, Surface functionalization of biomaterials by radical polymerization, Prog. Mater. Sci. 83 (2016) 191–235.
- [17] W. Lei, K. Ren, T. Chen, X. Chen, B. Li, H. Chang, J. Ji, Polydopamine nanocoating for effective photothermal killing of bacteria and fungus upon near-infrared irradiation, Adv. Mater. Interfaces 3 (2016) 1–6.
- [18] Y. Liu, K. Ai, L. Lu, Polydopamine and its derivative materials: synthesis and promising applications in energy, environmental, and biochemical fields, Chem. Rev. 114 (2014) 5057–5115.
- [19] E. Ju, K. Dong, Z. Liu, F. Pu, J. Ren, X. Qu, Tumor microenvironment activated photothermal strategy for precisely controlled ablation of solid tumors upon NIR irradiation, Adv. Funct. Mater. 25 (2015) 1574–1580.
- [20] M. Natan, F. Edin, N. Perkas, G. Yacobi, I. Perelshtein, E. Segal, A. Homsy, E. Laux, H. Keppner, H. Rask-Andersen, A. Gedanken, E. Banin, Two are better than one: combining ZnO and MgF₂ nanoparticles reduces *Streptococcus pneumoniae* and *Staphylococcus aureus* biofilm formation on cochlear implants, Adv. Funct. Mater. 26 (2016) 2473–2481.
- [21] F. Vatansever, W.C.M.A. de Melo, P. Avci, D. Vecchio, M. Sadasivam, A. Gupta, R. Chandran, M. Karimi, N.A. Parizotto, R. Vin, G.P. Tegos, M.R. Hamblin, Antimicrobial strategies centered around reactive oxygen species bactericidal antibiotics, photodynamic therapy, and beyond, FEMS Microbiol. Rev. 37 (2013) 955–989.
- [22] W. Yin, J. Yu, F. Lv, L. Yan, L.R. Zheng, Z. Gu, Y. Zhao, Functionalized Nano-MoS₂ with peroxidase catalytic and near-infrared photothermal activities for safe and synergetic wound antibacterial applications, ACS Nano 10 (2016) 11000–11011.
- [23] W.Y. Pan, C.C. Huang, T.T. Lin, H.Y. Hu, W.C. Lin, M.J. Li, H.W. Sung, synergistic antibacterial effects of localized heat and oxidative stress caused by hydroxyl radicals mediated by graphene/iron oxide-based nanocomposites, nanomedicine nanotechnology, Biol. Med. 12 (2016) 431–438.
- [24] S. Roy, S. Khanna, K. Nallu, T.K. Hunt, C.K. Sen, Dermal wound healing is subject to redox control, Mol. Ther. 13 (2006) 211–220.
- [25] G. Zhu, Q. Wang, S. Lu, Y. Niu, Hydrogen peroxide: a potential wound therapeutic target?, Med Princ. Pract. 26 (2017) 301–308.
- [26] M.D. Labas, C.S. Zalazar, R.J. Brandi, A.E. Cassano, Reaction kinetics of bacteria disinfection employing hydrogen peroxide, Biochem. Eng. J. 38 (2008) 78–87.
- [27] L. Gao, K.M. Giglio, J.L. Nelson, H. Sondermann, A.J. Travis, Ferromagnetic nanoparticles with peroxidase-like activity enhance the cleavage of biological macromolecules for biofilm elimination, Nanoscale 6 (2014) 2588–2593.
- [28] F. Natalio, R. André, A.F. Hartog, B. Stoll, K.P. Jochum, R. Wever, W. Tremel, Vanadium pentoxide nanoparticles mimic vanadium haloperoxidases and thwart biofilm formation, Nat. Nanotechnol. 7 (2012) 530–535.
- [29] Z.M. Markovic, B.Z. Ristic, K.M. Arsikin, D.G. Klisic, L.M. Harhaji-Trajkovic, B.M. Todorovic-Markovic, D.P. Kepic, T.K. Kravic-Stevovic, S.P. Jovanovic, M.M. Milenkovic, D.D. Milivojevic, V.Z. Bumbasirevic, M.D. Dramicanin, V.S. Trajkovic, Graphene quantum dots as autophagy-inducing photodynamic agents, Biomaterials 33 (2012) 7084–7092.
- [30] M.L. Brongersma, N.J. Halas, P. Nordlander, Plasmon-induced hot carrier science and technology, Nat. Nanotechnol. 10 (2015) 25–34.
- [31] S. Wilhelm, A.J. Tavares, Q. Dai, S. Ohta, J. Audet, H.F. Dvorak, W.C.W. Chan, Analysis of nanoparticle delivery to tumours, Nat. Rev. Mater. 1 (2016) 1–12.

- [32] H.Y. Kim, H.M. Lee, G. Henkelman, CO oxidation mechanism on CeO₂supported Au nanoparticles, J. Am. Chem. Soc. 134 (2012) 1560–1570.
- [33] S. Li, L. Xu, W. Ma, X. Wu, M. Sun, H. Kuang, L. Wang, N.A. Kotov, C. Xu, Dual-mode ultrasensitive quantification of MicroRNA in living cells by chiroplasmonic nanopyramids self-assembled from gold and upconversion nanoparticles, J. Am. Chem. Soc. 138 (2016) 306–312.
- [34] L. Treccani, T. Yvonne Klein, F. Meder, K. Pardun, K. Rezwan, Functionalized ceramics for biomedical, biotechnological and environmental applications, Acta Biomater. 9 (2013) 7115–7150.
- [35] H. Yu, J. Peng, Y. Xu, J. Chang, H. Li, Bioglass activated skin tissue engineering constructs for wound healing, ACS Appl. Mater. Interfaces 8 (2016) 703–715.
- [36] K. Li, J. Wang, X. Liu, X. Xiong, H. Liu, Biomimetic growth of hydroxyapatite on phosphorylated electrospun cellulose nanofibers, Carbohydr. Polym. 90 (2012) 1573–1581.
- [37] H.M. Song, D.H. Anjum, R. Sougrat, M.N. Hedhili, N.M. Khashab, Hollow Au@Pd and Au@Pt Core-shell nanoparticles as electrocatalysts for ethanol oxidation reactions, J. Mater. Chem. 22 (2012) 25003–25010.
- [38] X. Liu, H.C. Man, Laser fabrication of Ag-HA nanocomposites on Ti6Al4V implant for enhancing bioactivity and antibacterial capability, Mater. Sci. Eng. C 70 (2017) 1–8.
- [39] Z. Wang, C. Dong, S. Yang, D. Zhang, K. Xiao, X. Li, Facile incorporation of hydroxyapatite onto an anodized Ti surface via a mussel inspired polydopamine coating, Appl. Surf. Sci. 378 (2016) 496–503.
- [40] Y.Z. Zhou, Y. Cao, W. Liu, C.H. Chu, Q.L. Li, Polydopamine-induced tooth remineralization, ACS Appl. Mater. Interfaces 4 (2012) 6901–6910.
- [41] G.R. Alas, R. Agarwal, D.M. Collard, A.J. García, Peptide-functionalized poly [oligo (ethylene glycol) methacrylate] brushes on dopamine-coated stainless steel for controlled cell adhesion, Acta Biomater. 59 (2017) 108–116.
- [42] F. Ren, C. Zhai, M. Zhu, C. Wang, H. Wang, D. Bin, J. Guo, P. Yang, Y. Du, Facile synthesis of PtAu nanoparticles supported on polydopamine reduced and modified graphene oxide as a highly active catalyst for methanol oxidation, Electrochim. Acta 153 (2015) 175–183.
- [43] J. Li, L. Tan, X. Liu, Z. Cui, X. Yang, K.W.K. Yeung, P.K. Chu, S. Wu, Balancing bacteria-osteoblast competition through selective physical puncture and biofunctionalization of ZnO/polydopamine/arginine-glycine-aspartic acidcysteine nanorods, ACS Nano 11 (2017) 11250–11263.
- [44] Y. Jv, B. Li, R. Cao, Positively-charged gold nanoparticles as peroxidiase mimic and their application in hydrogen peroxide and glucose detection, Chem. Commun. 46 (2010) 8017–8019.
- [45] Y. Wen, L. Yan, Y.C. Ling, The designing strategies of graphene-based peroxidase mimetic materials, Sci. China Chem. 61 (2018) 266–275.
- [46] K.I. Ishibashi, A. Fujishima, T. Watanabe, K. Hashimoto, Detection of active oxidative species in TiO₂ photocatalysis using the fluorescence technique, Electrochem. Commun. 2 (2000) 207–210.
- [47] S.H. Kim, E.B. Kang, C.J. Jeong, S.M. Sharker, I. In, S.Y. Park, Light controllable surface coating for effective photothermal killing of bacteria, ACS Appl. Mater. Interfaces 7 (2015) 15600–15606.
- [48] D.K. Roper, W. Ahn, M. Hoepfner, Microscale heat transfer transduced by surface plasmon resonant gold nanoparticles, J. Phys. Chem. C 111 (2007) 3636–3641.
- [49] K. Brudzynski, K. Abubaker, D. Miotto, Unraveling a mechanism of honey antibacterial action: polyphenol/H₂O₂-induced oxidative effect on bacterial cell growth and on DNA degradation, Food Chem. 133 (2012) 329–336.
- [50] Y. Zhang, X. Liu, Z. Li, S. Zhu, X. Yuan, Z. Cui, X. Yang, P.K. Chu, S. Wu, Nano Ag/ ZnO-incorporated hydroxyapatite composite coatings: highly effective infection prevention and excellent osteointegration, ACS Appl. Mater. Interfaces 10 (2018) 1266–1277.
- [51] A.R. Deokar, L.Y. Lin, C.C. Chang, Y.C. Ling, Single-walled carbon nanotube coated antibacterial preparation and mechanistic study, J. Mater. Chem. B 1 (2013) 2639–2646.
- [52] M.N.M. Walter, K.T. Wright, H.R. Fuller, S. MacNeil, W.E.B. Johnson, Mesenchymal stem cell-conditioned medium accelerates skin wound healing: an in vitro study of fibroblast and keratinocyte scratch assays, Exp. Cell Res. 316 (2010) 1271–1281.
- [53] D. Hafner, L. Ziegler, M. Ichwan, T. Zhang, M. Schneider, M. Schiffmann, C. Thomas, K. Hinrichs, R. Jordan, I. Amin, Mussel-inspired polymer carpets: direct photografting of polymer brushes on polydopamine nanosheets for controlled cell adhesion, Adv. Mater. 28 (2016) 1489–1494.
- [54] S. Barrientos, O. Stojadinovic, M.S. Golinko, H. Brem, M. Tomic-Canic, Growth factors and cytokines in wound healing, Wound Repair Regen. 16 (2008) 585– 601.
- [55] C. Mao, Y. Xiang, X. Liu, Z. Cui, X. Yang, K.W.K. Yeung, H. Pan, X. Wang, P.K. Chu, S. Wu, Photo-inspired antibacterial activity and wound healing acceleration by hydrogel embedded with Ag/Ag@AgCI/ZnO nanostructures, ACS Nano 11 (2017) 9010–9021.